Additive Manufacturing 25 (2019) 511–521

Contents lists available at ScienceDirect

Additive Manufacturing

journal homepage: www.elsevier.com/locate/addma

Full Length Article

Experiments and simulations on solidification microstructure for Inconel 718 in powder bed fusion electron beam additive manufacturing

G.L. Knapp[a,*], N. Raghavan[b], A. Plotkowski[b], T. DebRoy[a]

[a] Department of Materials Science and Engineering, Pennsylvania State University, University Park, PA, United States
[b] Oak Ridge National Laboratory, Knoxville, TN, United States

ARTICLE INFO

Keywords:
Solidification
Additive manufacturing
Nickel-base superalloy
Electron beam
Microstructure

ABSTRACT

Previous research on the powder bed fusion electron beam additive manufacturing of Inconel 718 has established a definite correlation between the processing conditions and the solidification microstructure of components. However, the direct role of physical phenomena such as fluid flow and vaporization on determining the solidification morphology have not been investigated quantitatively. Here we investigate the transient and spatial evolution of the fusion zone geometry, temperature gradients, and solidification growth rates during pulsed electron beam melting of the powder bed with a focus on the role of key physical phenomena. The effect of spot density during pulsing, which relates to the amount of heating of the build area during processing, on the columnar-to-equiaxed transition of the solidification structure was studied both experimentally and theoretically. Predictions and the evaluation of the role of heat transfer and fluid flow were established using existing solidification theories combined with transient, three-dimensional numerical heat transfer and fluid flow modeling. Metallurgical characteristics of the alloy's solidification are extracted from the transient temperature fields, and microstructure is predicted and validated using optical images and electron backscattered diffraction data from the experimental results. Simulations show that the pure liquid region solidified quickly, creating a large two-phase, mushy region that exists during the majority of solidification. While conductive heat transfer dominates in the mushy region, both the pool geometry and the solidification parameters are affected by convective heat transfer. Finally, increased spot density during processing is shown to increase the time of solidification, lowering temperature gradients and increasing the probability of equiaxed grain formation.

1. Introduction

Controlled solidification is important for the processing of nickel-base superalloy Inconel 718 (IN718) to achieve superior mechanical properties. However, traditional manufacturing processes often necessitate a choice between columnar and equiaxed grains for a single part. For example, directionally solidified castings aim to create columnar or single-crystal alloys with exceptional high-temperature properties while wrought alloys with equiaxed grains can be employed at moderate operating temperatures [1,2]. Additionally, because equiaxed grains are considered defects during directionally solidification, control over the suppression of stray equiaxed grains during columnar grain growth is crucial to reliable directionally solidified parts. Recent developments in powder bed fusion electron beam (PBF-EB) additive manufacturing (AM) show the promise of pulsed melting scanning patterns to both suppress or promote equiaxed grain formation during AM by controlling local processing parameters [3–7]. Combined with the geometric freedom that AM provides, these advances have potential to offer another level of design to engineered AM parts [8].

Despite experimental advances that show control of IN718 microstructure through PBF-EB with pulsed melting scanning strategies, transient and spatial variations during solidification make it a difficult process to understand from a metallurgical perspective. For alloys undergoing dendritic solidification, typical of AM, a columnar to equiaxed transition (CET) occurs in response to changes in the solidification parameters, such as local temperature gradients and the speed of the solidification front. Building on theoretical understanding of the CET from Hunt [9], Kurz et al. [10], and others [11,12], a significant amount of research on a variety of materials has been done to correlate processing parameters with the final grain structure. Specifically for IN718, Raghavan et al. presented a qualitative correlation between numerical models calculating heat conduction during processing and actual microstructures formed during processing [13]. Other work used

* Corresponding author.
E-mail address: glk9@psu.edu (G.L. Knapp).

https://doi.org/10.1016/j.addma.2018.12.001
Received 12 September 2018; Received in revised form 16 November 2018; Accepted 2 December 2018
Available online 05 December 2018

similar modeling for quantitative comparison between the predicted and measured primary dendritic arm spacing [5,14]. For other widely used AM alloys and scanning strategies, more aspects of the PBF-EB process have been investigated. Notably, fluid flow and vaporization were considered in a multi-physics model for PBF-EB [15] that was applied by Thorsten et al. to calculate grain growth of Ti-6Al-4 V as a function of various process parameters [16].

These efforts to understand grain growth in PBF-EB processing have produced a conclusive link between processing parameters and microstructural features. Importantly, details of the heat source, such as power and scanning strategy, have been shown to have a strong connection to defects [16,17] and the direction of temperature gradients and grain growth [18–20]. However, despite the understanding generated by previous research, the underlying role of the various physical phenomena that determine solidification parameters, such as fluid flow and vaporization, have yet to be specifically investigated for pulsed melting PBF-EB AM.

These physical phenomena are important when determining the appropriate processing parameters through either experiments or through numerical simulations. It is well known in fusion welding and laser processing applications that liquid metal flow is driven by gradients in surface tension in the pool (*i.e.,* Marangoni effect) and allows for heat to be carried by fluid flow [21,22]. Driven by the Marangoni effect, heat transfer by fluid flow could change the solidification parameters drastically. In laser-based powder bed fusion, it has been shown that fluid flow reduces temperature gradients and decreases the peak temperature within the molten pool for Stainless Steel 316 alloy [23]. Similar results were also shown for laser-based directed energy deposition [24]. It is necessary to understand how these effects play a role in PBF-EB of IN718, especially when models neglecting fluid flow are used in literature [13,14,25,26] for ease of implementation and lower computational costs.

This study investigates the role of fluid flow and vaporization during the PBF-EB of IN718 alloy using a pulsed electron beam scanning strategy that has been previously shown to offer localized control over microstructure [3–7]. The impact of these phenomena on the solidification microstructure of the alloy is investigated, specifically considering the evolution of the fusion zone geometry, and the spatially and temporally dependent temperature gradients and solidification growth rates. Temperature and velocity profiles and the resultant solidification parameters are calculated numerically from a transient three-dimensional heat transfer and fluid flow model. Furthermore, experiments were conducted using PBF-EB of IN718 to help validate the model results and to examine the effect of spot density during a pulsed scanning pattern on the resultant solidification morphology. Microstructural morphology was determined through electron backscattered diffraction (EBSD) imaging and the development of the resultant microstructure was explained by examining the predicted columnar-to-equiaxed transition from corresponding numerical results.

2. Methods

2.1. Modelling of transient temperature and velocity fields

Heat transfer and fluid flow during PBF-EB processing was simulated using an iterative solution of the equations for conservation of mass, momentum, and energy in a transient three-dimensional form [27,28]. Following the finite difference method, discretization of the governing equations into control volumes formed the framework for the calculations. In each iteration, the governing equations were solved sequentially for enthalpy, 3-D velocity components, and pressure. Hence, a solution was arrived at iteratively using the semi-implicit method for pressure-linked equations (SIMPLE). This procedure is repeated for each time-step to produce transient solutions. The details of the numerical methods used in this model are detailed thoroughly by Patankar [29] and in earlier works for laser welding [27,28,30], so only the aspects unique to this version of the model are discussed in detail. Descriptions of the governing equations are provided in Supplement C.

To focus the scope of the study, several key assumptions are made in this model.

1 The properties of the powder layer are taken to be the same as bulk material. The powder layers in this study are approximately one to two powder particles, because the layer thickness is 50 μm and powder diameters are 45–105 μm. While powder bed thermal conductivity can vary significantly from bulk properties [26], sintering of the powder particles before each layer increases the thermal and electrical conductivity of the powder bed by increasing particle-to-particle and particle-to-substrate contact area [31].
2 Material emissivity is assumed to be constant.
3 For in-depth analysis of the physical phenomena involved, only the melting from a single electron beam pulse is considered. Preliminary simulations informed the appropriate initial and boundary conditions for simulating this subset of the entire electron beam melting process, shown in the supplementary material.

For modeling of a single electron beam pulse, the initial condition of the domain is set to a specified temperature to replicate the preheating/sintering step present in real PBF-EB systems, as well as to simulate substrate heating during processing. In this study, experimental samples were made, one with higher energy density and one with lower energy density during processing using a pulsed electron beam scanning pattern. Preliminary simulations showed that the lower energy density allowed the region around each spot to cool down to near the build chamber temperature (1273 K) between melting of neighboring spots. In the case of the higher energy density, these simulations showed the build area increased in temperature to nearly 1500 K. Therefore, an initial domain temperature of 1273 K was used for the lower energy density case and 1500 K for the higher energy density case.

Additionally, only a subset of the full build area used in actual processing is simulated for validation against experimental data. This is done to reduce computational complexity, as the influence of melting far away from the region of interest does not affect results significantly within the simulated time frames. The scanning pattern used is the same as described in the experimental section, and no heat input is used for any time the beam is located outside the simulated region of interest. For all other analyses, only a single spot was simulated to eliminate variability that may be introduced by the scanning pattern.

Table 1 presents further details about the simulation parameters, with materials properties taken from literature [21,32,33]. Because the layer thickness was of the same order of magnitude as the powder diameter and the pool depth was much larger than the layer thickness,

Table 1
Material properties for Inconel 718 alloy [21,32,33].

Material property	
Density	8.1 g/cm^3
Dynamic viscosity	0.00531 Pa s
Solidus (T_S)	1533 K
Liquidus (T_L)	1609 K
Boiling point (T_B)	3120 K
Latent Heat of Fusion	209.2 J/g
Surface tension (γ)	1820 mN/m
$d\gamma/dT$	−0.37 mN/m K
$c_p(T)$	$3.6 + 2.5 \times 10^6 \times T - 4.0 \times 10^{-8} \times T^2$ J/gK
$c_p(T_S)$	0.668 J/g K
$c_p(T_L)$	0.728 J/g K
$k(T)$	$5.6 \times 10^{-1} + 2.9 \times 10^{-2} \times T - 7.0 \times 10^{-6} \times T^2$ $W/m.K$
$k(T_S)$	0.292 W/m K
$k(T_L)$	0.296 W/m K
Liquid viscosity	0.0531 g/cm s
Emissivity	0.5

Table 2
Simulation parameters.

Parameter	
Powder material	IN718
Beam current	20 mA
Beam voltage	60 kV
Beam radius	400 μm
Time Beam On	0.25 ms
Layer thickness	50 μm
Substrate thickness	0.5 mm
Number of layers	1
Cooling time at end	200.0ms
Time step	0.0625 ms
Control volume size in fine-meshed region	10 μm (X) × 10 μm (Y) × 10 μm (Z)
Domain size (single spot)	2.5 mm (X) × 2.5 mm (Y) × 0.55 mm (Z)
Domain size (multiple spots)	5.0 mm (X) × 3.5 mm (Y) × 0.55 mm (Z)

the density in the growing layer was approximated as that of the liquid. A flat-surface approximation was made for the top surface of the substrate, because peak temperatures were shown to be below the boiling temperature of 3120 K and no keyhole should form. Therefore, surface deformation is expected to be minimal.

2.1.1. Electron beam characteristics

Simulation of PBF-EB requires the definition of a number of parameters, starting with the characteristics of the electron beam that determine the size and intensity of the heat source. From electron beam welding literature [34], the electron range, the distance where 99% of the electron beam's energy is absorbed, is defined as,

$$S \approx 2.1 \times 10^{-12} \frac{U_B^2}{\rho} \text{ for } 10 \text{ kV} < \text{UB} < 100\text{kV} \quad (1)$$

Material density (ρ, g/cm^3) and accelerating voltage (U_B, V) are considered constant. Using material property values provided in Table 1 and process parameters in Table 2, the electron range (S, cm) is approximately 9.3 μm.

Absorbed volumetric power density varies with depth non-linearly throughout the electron range. This can be approximated by the empirical relation [34],

$$p_d(z) = \frac{p_{A,max}}{h}\left[1 - \frac{9}{4}\left(\frac{z}{S} - \frac{1}{3}\right)^2\right] \quad (2)$$

Here, the maximum power intensity ($p_{A,max}$, W/cm^2) is taken as the total input power, after all energy losses are included, divided by the incident beam area. Depth-varying power density (p_d, W/cm^3) varies with the depth from the surface of the workpiece (z, cm) compared to the electron range (S, cm) and the height of the discrete volume being considered (h, cm).

The power density also varies radially, and due to a lack of experimental characterization it is approximated as a Gaussian beam. Therefore, the input power density can be fully described as,

$$p_V(r, z) = p_d(z) e^{-r^2/r_B^2} \quad (3)$$

The depth-varying volumetric power density (p_d, W/cm^3) is multiplied by a function of the distance from the center of the beam (r, cm) divided by the radius of the beam (r_B, cm) to obtain the input power density (p_V, W/cm^3).

2.1.2. Energy losses and vaporization

Multiple sources of energy loss are considered in calculating the total absorbed power by the volumetric heat source. During PBF-EB processing, metal vapor has been shown to form in sufficient quantities capable of creating metallic films on surfaces in the build chamber [3]. In a high vacuum, the electron beam would travel unimpeded, but due to interactions with metal vapor some beam current will be lost [35] and the beam's focal point will shift closer to the lens causing the incident beam diameter to increase [36]. Within the PBF-EB system used, there is no quantitative understanding of the beam-vapor interaction, nor of the effect of the focus coil current on beam diameter. Therefore, the model used in this work takes into account a more diffuse beam by considering the beam diameter to be 400 μm, two times larger than the approximate diameter of the fully focused electron beam. Furthermore, energy lost from backscattered electrons is taken to be 30% of the total power incident to the substrate, based on the alloying elements present in IN718 [34].

The material surrounding the domain side and bottom surfaces is taken to be IN718 alloy at 1273 K for the low energy density case and 1500 K for the high energy density case. Heat loss from these domain walls is calculated by heat conduction from boundary-adjacent cells to the boundary cells. Radiative heat loss was assigned to the top surface boundary based on the top-surface temperature and a temperature-independent emissivity value was approximated as 0.5 [33]. Finally, based on the temperatures in the molten pool, the partial equilibrium vapor pressures for each alloying element were calculated [37] and applied to a variation on the Langmuir equation to calculate the vaporization mass flux [22,38]. Combining the vaporized mass flux with the heat of vaporization results in an equation for heat loss from the surface [39]:

$$H_{loss} = \sum_{i=1}^{n} \left[44.33 \Delta H_i P_i \sqrt{\frac{A_i}{T}}\right] \quad (4)$$

In the above equation, the total heat flux (H_{loss}, cal/s. cm^2) is the sum of the heat flux for each of the n elements within the alloy. For an element i, heat flux is calculated from the equilibrium vapor pressure (P_i, atm), the atomic weight (A_i, g/mol), the heat of vaporization (ΔH_i, cal/g), and the temperature at the given location (T, K). The constant provides for the appropriate unit conversions. Table 3 presents material properties used for calculating vaporization heat loss [37,40].

Table 3
Composition of Inconel 718 and parameters for vaporization heat loss considered in the model. The chemical composition was taken from the ranges provided by the manufacturer [40] and physical data for Inconel 718 literature [37].

Element	Quantity (wt. %)	Boiling point (K)	Heat of vaporization (kJ/mol)
Ti	0.90	3558	425.8
Al	0.50	2793	290.9
Fe	16.85	3133	340.4
Cr	19.0	2945	342.1
Ni	52.5	3183	374.3
Mn	0.35	2333	231.1
Cu	0.30	2833	304.8
Si	0.35	3543	384.8
Mo	3.05	4883	590.3
Nb	5.20	5013	683.7
Co	1.00	2930	375.0

Composition is taken from allowable ranges of IN718 alloy, as specified by the manufacturer.

2.2. Solidification calculations

The transient temperature distribution within two-phase region, commonly referred to as the mushy zone, must be examined to determine temperature gradients, solidification front velocities, and derivative solidification parameters. From the single pool simulation, extracted values for both the temperature gradients and solidification rates at the solid/mushy interface are used to calculate other important solidification parameters that determine microstructural features. The temperature gradient is taken as the average gradient in the mushy zone, because the temperature gradient was shown to have a constant spatial gradient of temperature within the mushy zone during simulations. This reduces the effects of mesh-size when taking gradients across small distances at an interface. As the model is at the continuum-scale, individual dendrites are not simulated and the solidification growth rate is approximated as the change in position of the solid/mushy interface every time-step. Because the spatial gradient of temperature is constant across the mushy zone in the simulations presented here, it is also assumed that solidification growth rates are constant across the mushy zone such that the solid/mushy interface velocity is a representative value for the entire region. For notation, in the radial direction along the top-surface, the radius of the molten pool's solid/mushy interface is r_S. In the depth direction, along the centerline down through the pool, the depth of the solid/mushy interface is d_S. The temperature gradient (G) and the solidification front velocity (R) along the radial direction are therefore noted as G_r and R_r, and as G_d and R_d along the depth centerline. The derived solidification parameters GR and G/R were obtained from the computed transient temperature field. The instantaneous cooling rate, GR, represents the cooling rate at the solid/mushy interface at a particular time, and the parameter G/R determines the microstructural morphology.

Alloys with several alloying elements, such as IN718, typically have large solidification ranges. This leads to an undercooled region which either propagates stably as a planar front or unstably as cellular or dendritic structures [10,41]. The constitutional supercooling criterion states that the solidification front will be unstable if the following condition is met:

$$G/R < \Delta T_{eq}/D_L \tag{5}$$

The ratio of temperature gradient (G, K/m) and the solidification front velocity (R, m/s) is compared to the ratio of the solidification range of the alloy (ΔT_{eq}, K) and the solute diffusivity in the liquid (D_L, m^2/s). The diffusivity of niobium in liquid nickel is assumed to be a representative solute diffusivity. Data in Table 4 from the literature suggest that the solidification morphology of IN718 in PBF-EB processing was either cellular or dendritic depending on the processing conditions [3,13,21,42,43].

For dendritic solidification, it is possible to have either epitaxial columnar grain growth from the solidification front or equiaxed grains nucleating ahead of the solidification front. The determination of the columnar to equiaxed transition (CET) has received detailed treatment [9,12,44], so only an abbreviated summary is reproduced here. For temperature gradients and solidification rates typically reported in PBF-EB [6,21], the thickness of the region where equiaxed grains can form ahead of the solidification front is necessarily small. Therefore, the nuclei density dominates equiaxed grain formation and the role of nucleation undercooling on equiaxed dendrite growth can be neglected [9]. In all cases, the undercooling of the dendrite tip drives the dendritic growth. To avoid solving concentration fields and to determine the exact constitutional undercooling around the dendrite tip, an empirical relation is commonly used [12]:

$$\Delta T = (a \bullet V)^{1/n} \tag{6}$$

Here, the undercooling of the dendrite tip (ΔT, K) is related to the dendrite tip velocity (V, m/s) and the material-dependent parameters a and n. The parameter a is a scaling factor associated with the amount of undercooling needed to induce the CET in the alloy. The parameter n is a constant that is taken from the slope of the CET curves of a solidification map. To compute both a and n from a solidification map, it is necessary to consider geometric arguments proposed by Kurz et al. [45] which necessitate that a critical temperature gradient exists for fully equiaxed grain growth,

$$G_c = N_0^{1/3} \Delta T \tag{7}$$

Here, the critical temperature gradient (G_c, K/m) is related to nuclei density (N_0, m^{-3}) and undercooling (ΔT, K) by equating the length of the undercooled zone and distance between two nuclei. This corresponds to the temperature gradient where equiaxed grains will fully block columnar grain growth.

Once the empirical constants have been calculated, the volume fraction of the equiaxed grains must be determined to know if there is sufficient equiaxed grain nucleation to block columnar growth. First, the radius of the equiaxed grains is obtained by integration of the dendrite tip velocity over time:

$$r = \int_0^t V dt \tag{8}$$

This can be related to dendrite tip undercooling, temperature gradient, and dendrite tip velocity by assuming steady-state growth for equiaxed dendrites:

$$d(\Delta T)/dt = -VG \tag{9}$$

The change in dendrite tip undercooling (ΔT, K) over time is equivalent to the negative value of dendrite tip velocity (V, m/s) multiplied by temperature gradient (G, K/m). Combining Eqs. (6)–(9) and integrating allows for the relation of G and V with equiaxed grain radius:

$$G = \frac{1}{n+1}\left(\frac{1}{r}\right)(aV)^{1/n} \tag{10}$$

Assuming a spherical shape and using the concept of extended volume fraction with the Avrami equation allows for the volume fraction of equiaxed grains, ϕ, to be calculated:

$$\phi = 1 - \exp\left(-\frac{4}{3}\pi r^3 N_0\right) \tag{11}$$

Finally, combining Eqs. (10) and (11) allows for the volume fraction of equiaxed grains produced during solidification to be related to the primary solidification parameters and material-dependent parameters. This leads to the equation presented by Gäumann et al. [12]:

$$\frac{G^n}{V} = a\left[\frac{1}{n+1}\left(\frac{-4}{3}\frac{\pi N_0}{\ln(1-\phi)}\right)^{\frac{1}{3}}\right]^n \tag{12}$$

As proposed by Hunt [9], $\phi < 0.0066$ is considered fully columnar growth and $\phi > 0.49$ is considered fully equiaxed growth. This can be used to calculate critical values of G^n/V for determining grain

Table 4
Parameters for solidification plane front stability during PBF-EB of Inconel 718.

Parameter	
D_L (Nb in liquid Ni) [42]	3.0×10^{-9} m^2/s
ΔT_{eq} for IN718	76 K
Typical G [3,13,21]	10^5–10^6 K/m
Typical R [3,13,21]	10^{-3}–10^{-1} m/s
Typical G/R	10^6–10^9 K s/m^2
G/R for plane front stability	$> 2.5 \times 10^{10}$ K s/m^2

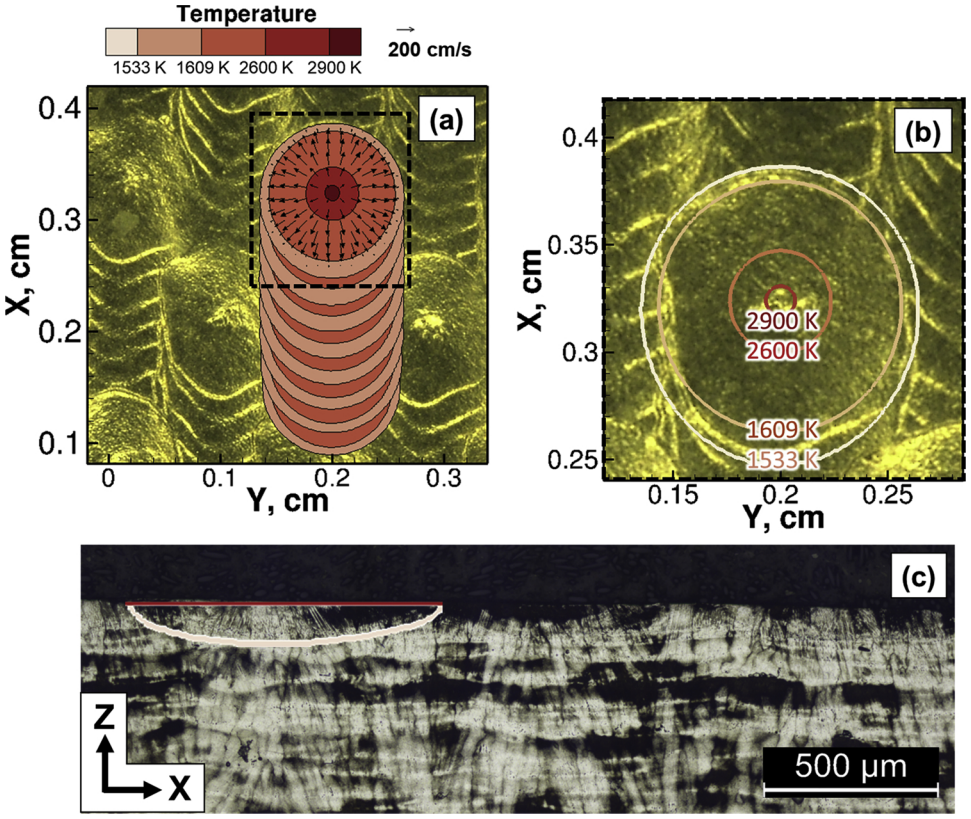

Fig. 1. Simulated molten pool shapes overlaid on optical images of the columnar-grained sample using the parameters for multiple spots in Table 3. (a) Multiple molten pool boundaries overlaid to show overlap between pools and elongated pool shape. (b) Closer view of region bound by dotted box with isotherms denoting the largest pool geometry formed at that spot. (c) Transverse section of the XZ plane with overlaid solidus isotherm corresponding to observable pool boundaries.

morphology. The dendrite growth rate (V) is assumed to be the same as the solidification front velocity (R) for simplicity. Nastac et al. developed a solidification map of IN718 for casting of thin-walled parts [46], which includes similar temperature gradients and solidification growth rates used in PBF-EB processing. Combining this with Eqs. (6)–(12), the constants required to use these methods are derived as $n = 2$, $a = 4.5\,K^2s/m$, and $N_0 = 2.65 \times 10^{14}\,m^{-3}$. Further details of these calculations are provided in Supplement B. Therefore, the condition for fully equiaxed grains formation is $\frac{G^2}{R} < 6.98 \times 10^9 K^2s/m^3$ and the condition for fully columnar grain formation is $\frac{G^2}{R} > 1.52 \times 10^{11} K^2s/m^3$. In-between these two regions, mixed columnar/equiaxed grains should be observed.

2.3. Experimental methods

To fabricate the experimental samples, a PBF-EB additive manufacturing system (Arcam® S12) at the Manufacturing Demonstration Facility (MDF) in Oak Ridge National Laboratory (ORNL) was used. Gas atomized IN718 powder (-106/ + 45 μm) was used to fabricate the samples. The samples were produced using a spot melting pattern described by Raghavan et al. [13]. Instead of the typical line-based scanning pattern, the beam rapidly pulsed to melt individual spots across a 20 mm x 20 mm build area. Using this method with a layer thickness of 50 μm, cubes with a side length of 20 mm were built. Distance between neighboring spots controls the energy density for a particular area, therefore spot densities of 16 spots/mm^2 and 36 spots/mm^2 were used to obtain lower and higher energy densities, respectively. The entire area was covered in multiple passes, with spots in the same pass being in a grid with 3.0 mm between them in the horizontal direction (x-axis) and 1.5 mm in the vertical direction (y-axis). When 16 spots/mm^2 were used, the grid for each sequential pass was shifted 250 μm horizontally, and on every twelfth pass the grid shifted vertically 250 μm, repeated until the entire build area was covered. When using 36 spot/mm^2 the horizontal and vertical shifts were 170 μm. These parameters were chosen based on earlier work by Raghavan et al. [5,13] to obtain columnar and equiaxed grain structures. To fabricate the samples, a beam current of 20 mA and beam diameter of 400 μm is used. It is noted that the beam diameter is supplied by the manufacturer and was not able to be experimentally verified. At each spot in a layer, the electron beam is turned on for 0.25 ms before moving to the next spot. Experimental characterization of other systems has shown that the beam diameter is sensitive to a number of machine parameters and varies depending on which machine is used [47].

After the build was completed, sections were taken through the middle planes of the samples, perpendicular to the top-surface of the sample. Sections were polished, then examined using optical and scanning electron microscopy. Electron beam backscatter diffraction (EBSD) was used to inspect the grain orientation of the sections to show typical grain morphologies.

3. Results and discussion

3.1. Evolution of pool geometry and temperature field

To validate model results against experiments, the spot scanning pattern described in the Experimental Methods section was simulated using parameters in Table 2. A section of the resulting temperature fields is shown as overlaid spots on the observed results in Fig. 1a. The liquidus (1609 K) and solidus (1533 K) contours are overlaid for each spot to show the scanning pattern and consistency with the experimental results. Zooming in on a single molten pool in Fig. 1b, good agreement is seen between the shape and size of the simulated results and the experiment, with nearly an exact match in the pool width and length compared to the experiment. Fig. 1c shows a transverse section of the same sample, with simulation results overlaid for a single spot. The solidus isotherm for IN718 shows a penetration depth matching the observable pool boundaries. Increasing the density of spots to 36 spots/mm^2 caused the individual pools to merge together, such that pool geometries were not visible via optical microscopy, making it infeasible

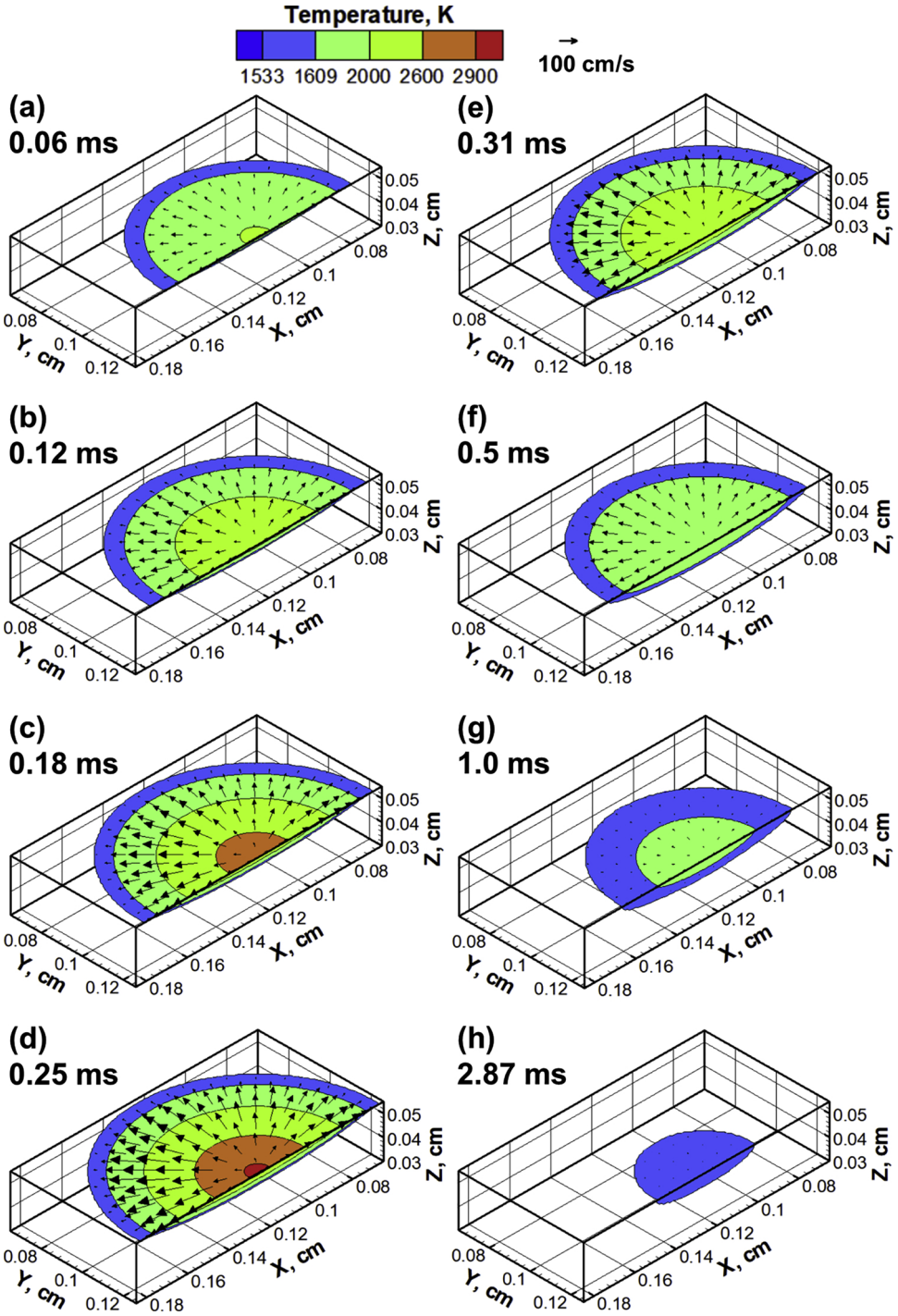

Fig. 2. (a–h) Transient temperature and velocity fields during the melting of a single spot using the parameters in Table 3 and an initial substrate temperature of 1273 K. (a–d) Heating during 0.0-0.25 ms (e–h) Cooling of the spot. All images use the same temperature contours and velocity vector scale, shown at the top of the figure.

to validate in a similar fashion. Optical images of all experimental results and a simulation video showing pool merging are available in the supplemental material.

Visualizing the development of a single spot within a spot-melting pattern provides a starting point to understand the melting and solidification process. Fig. 2 depicts a simulated pool that rapidly develops during 0.25 ms of being exposed to a stationary electron beam, which then cools after the beam is turned off. The large temperature gradients generated by the focused electron beam resulted in large surface tension gradients that caused fluid velocities on the surface of the pool to reach values upwards of 250 cm/s due to the Marangoni effect. Large radial velocities aided rapid radial expansion of the pool, while pool growth was relatively slow in the depth-direction, showing the importance of heat transfer by convection in determining the development of the pool geometry.

Due to the influence of these radial velocities, the transient size and shape of the molten pool are affected by fluid flow. Fig. 3 shows the comparison of the pool radius (r_s) and the pool depth (d_s) over time for simulations with and without fluid flow. These results show that the effect of fluid flow also has an influence on the rate at which the pool

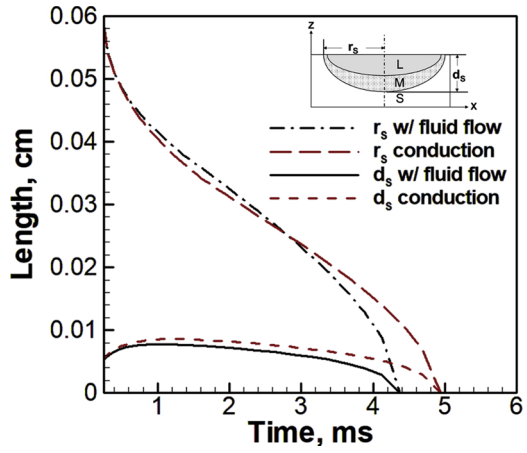

Fig. 3. Development of pool radius (r_S) and pool depth (d_S) over time for a single spot simulated using parameters in Table 3 and an initial substrate temperature of 1273 K. Inset figure shows schematic of the liquid metal pool (L), mushy zone (M), and solid metal (S). A comparison is made between results with fluid flow (black lines) and results only considering thermal conduction (red lines). X-axis starts at 0.25 ms, when the beam is turned off (For interpretation of the references to colour in this figure legend, the reader is referred to the web version of this article).

solidifies. Fluid flow caused the pool to solidify completely approximately 0.5 ms earlier than if fluid flow is ignored, which is 10% of the total cooling time. This means that the solidification rate of the pool will be lower if fluid flow is ignored during simulations.

Furthermore, the effect of fluid flow can also be seen in the spatial variation of the temperature, shown in Fig. 4. During heating, the temperature near the middle of the pool is approximately 100 K lower when considering fluid flow, Fig. 4a, than when ignoring fluid flow, Fig. 4c. This indicates again that heat is being carried away from the center by fluid convection, and also has implications during calculations of radiation heat loss and vaporization heat and mass losses. IN718 has a boiling point of approximately 3120 K, so an increase of peak temperature from 2900 K to 3000 K can have a significant effect on the vapor pressure of alloying elements above the molten pool. Enhanced vaporization heat losses combined with increased radiation heat losses due to this 100 K increase in peak temperature resulted in 10% less power being absorbed into the material overall, even though peak temperatures were higher. Additionally, the slope of the temperature contours during cooling while considering fluid flow, Fig. 4b, are less steep than during cooling while ignoring fluid flow, Fig. 4d. Therefore, ignoring fluid flow increases the spatial gradient of temperature.

The simulated development of the liquid/mushy interface and mushy/solid interface is shown in Fig. 5. It shows the distance from the center of the pool to the liquid/mushy interface (r_L), from the center of the pool to the mushy/solid interface (r_S), and the thickness of the mushy region (t_M) during the same single pool simulation presented in Fig. 2. Notably, the single-phase liquid region cools rapidly compared to the mushy zone, which leaves the entire molten pool containing a two-phase solid-liquid region for a majority of the solidification. This phenomenon occurs due to a number of factors. Firstly, because temperature gradients decrease over time, surface tension varies less across the molten pool and the driving force for Marangoni flow is reduced. Increased viscosity in the mushy region also contributes to reduced fluid flow, so consequently, heat transfers more slowly once the single-phase liquid has cooled completely to the two-phase region. Secondly, though a large amount of heat is put into the system in a short period of time, the latent heat released from the solidification of the alloy is significant. The raw input power of 1200 W, or 900 W after backscattering losses, leads to approximately 225 mJ of energy deposited into the substrate during the 0.25 ms of melting. This results in a maximum pool volume of 3.33×10^{-5} cm^3 during the simulation for Fig. 2. With IN718 having a density of 8.1 g/cm^3 and a latent heat of fusion of 209 J/g, roughly 60 mJ of energy was released during the solidification of the alloy. This was approximately 25% of the total energy input by the electron beam, so it was a significant amount of heat energy that contributed to slowed solidification through the mushy zone.

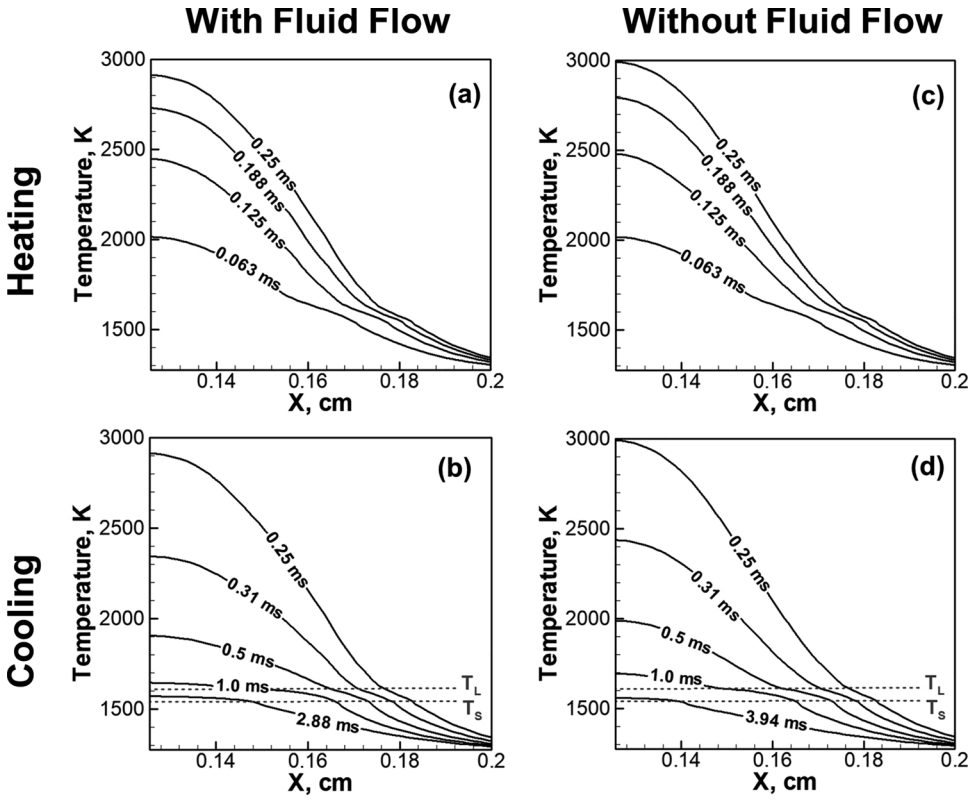

Fig. 4. Simulated transient temperature profiles on the top-surface of the molten pool for the results shown in Fig. 2, a single spot simulated using parameters in Table 3. (a) Heating and (b) cooling for simulations with fluid flow. Similarly, (c) heating and (d) cooling for simulations without fluid flow. The x-axis begins at the center of the pool (x = 0.125 cm) for all plots.

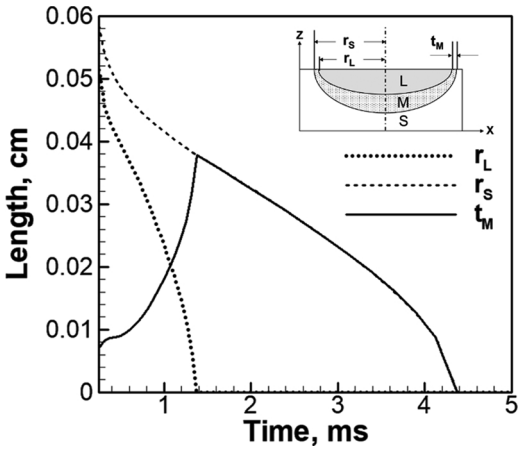

Fig. 5. Depiction of the radius of the solidus isotherm (r_S), liquidus isotherm (r_L), and the width of the mushy zone (t_M) for the simulation of a single-spot using parameters shown in Table 3 and an initial substrate temperature of 1273 K. X-axis starts at 0.25 ms, when the beam is turned off.

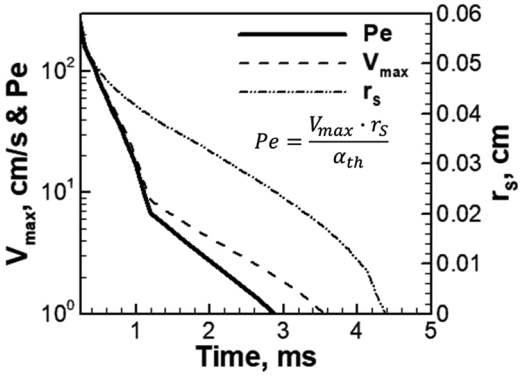

Fig. 6. Peclet number (Pe), maximum velocity (V_{max}), and pool radius (r_S) during the heating and the cooling of a single spot, using parameters from Table 3 and an initial substrate temperature of 1273 K. X-axis starts at 0.25 ms, when the beam is turned off.

To help quantify the influence of fluid flow and see how it changes with time, the Péclet number (Pe) was used. It is a dimensionless ratio between the heat transferred by convective fluid motion and the heat transferred by thermal conduction. If Pe is much greater than unity, than fluid flow is a significant contribution to heat transfer within the system. The Péclet number is defined as [48],

$$Pe = \frac{V_{max} r_S}{\alpha_{th}} \tag{13}$$

where r_S is the radius from the center of the pool to the mushy/solid interface, V_{max} is the maximum velocity in the pool, and α_{th} is the thermal diffusivity inside the pool. Fig. 6 indicates that $Pe > 10$ until approximately 1.5 ms after the beam is turned off (i.e., time = 1.75 ms). In this time period where Pe is high, the velocity dominates the changes in the Péclet number, as it changes orders of magnitude from 100 cm/s to 10 cm/s in less than one millisecond. In the same time period, the radius of the pool only decreases from 0.5 cm to 0.4 cm, which is less drastic of a change. The single-phase liquid region vanishes shortly after 1 ms, so convective heat transfer by fluid flow plays a significant role in heat transfer for the entire time when the single-phase liquid is present. Once the single-phase liquid cools into the two-phase region, the Péclet number is on the order of unity which means fluid flow is not the dominant mechanism of heat transfer during the cooling of the mushy zone. This analysis suggests that convective heat transfer is the dominant mechanism of heat transfer within the liquid pool. When the single-phase liquid region is replaced by the two-phase mushy zone

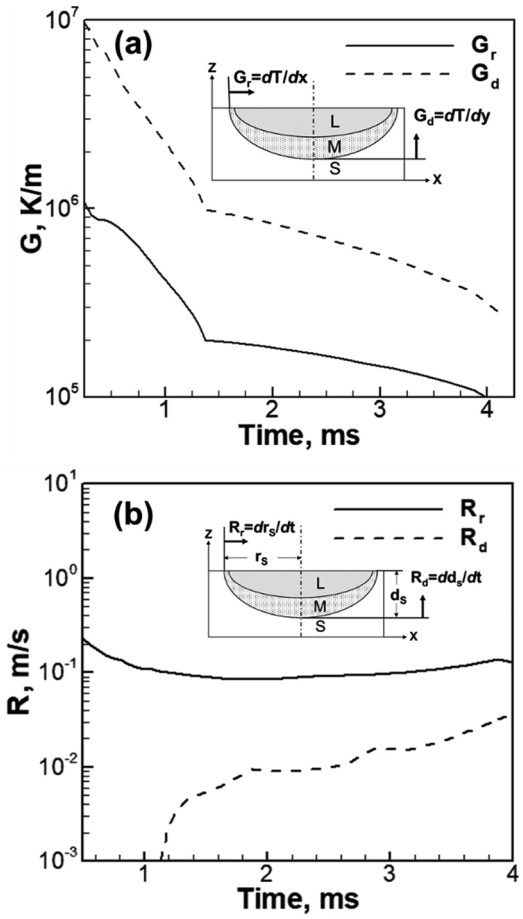

Fig. 7. Solidification parameters from the simulation of a single spot, using parameters in Table 3 and an initial substrate temperature of 1273K. (a) Transient temperature gradients, G, at the solidus isotherm and (b) solidification front velocity, R. The inset diagrams in each figure depict the subscript notation. X-axis starts at 0.25ms, when the beam is turned off.

during solidification, the role of convective heat transfer decreases progressively and heat conduction becomes important. The role of different modes of heat transfer need to be examined for every alloy system, since the thermophysical properties of the alloy such as the thermal conductivity, specific heat, the temperature coefficient of interfacial tension, and the temperature range of solidification strongly depend on the specific alloy.

3.2. Temporal variation of solidification parameters

Fig. 7 shows simulated values of G and R along the top-surface radial direction (G_r, R_r) compared to G and R along the depth-direction (G_d, R_d). Shown in Fig. 7a, the temperature gradient is much greater in the depth-direction. As heat is primarily carried in the radial direction by fluid flow, the temperature gradient in G_r is decreased compared to the depth-direction where fluid flow does not cause as vigorous mixing between the top and bottom of the molten pool. In Fig. 7b, the rate of solidification in the radial direction, R_r, is higher than in the depth-direction direction, R_d, for the same reason, because with radial fluid flow the material can dissipate heat more quickly. There is also a significant transient effect on the solidification parameters. Similar to what has been shown previously in laser spot welding [49], the temperature gradients decrease steadily over time and the solidification rate initially decreases followed by an increased rate as the pool shrinks. In the case of G_r, there is an order of magnitude change between the beginning and the end of solidification due to the dropping temperature inside the molten pool as solidification progresses.

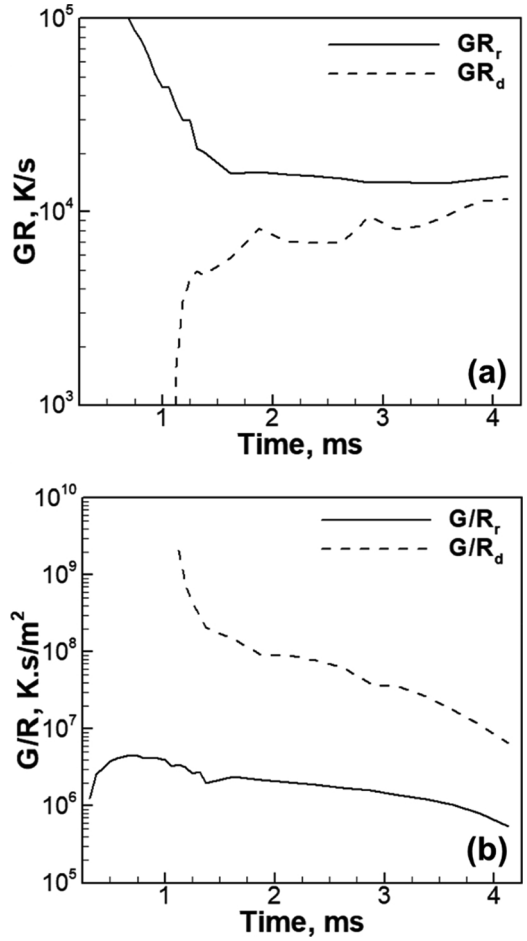

Fig. 8. Derived solidification parameters from simulation of a single spot using parameters from Table 3 and an initial substrate temperature of 1273 K. (a) Cooling rates, GR, at the solidus isotherm, calculated by multiplication of G and R. (b) Values of solidification parameter G/R, calculated by the quotient of G and R. X-axis starts at 0.25 ms, when the beam is turned off.

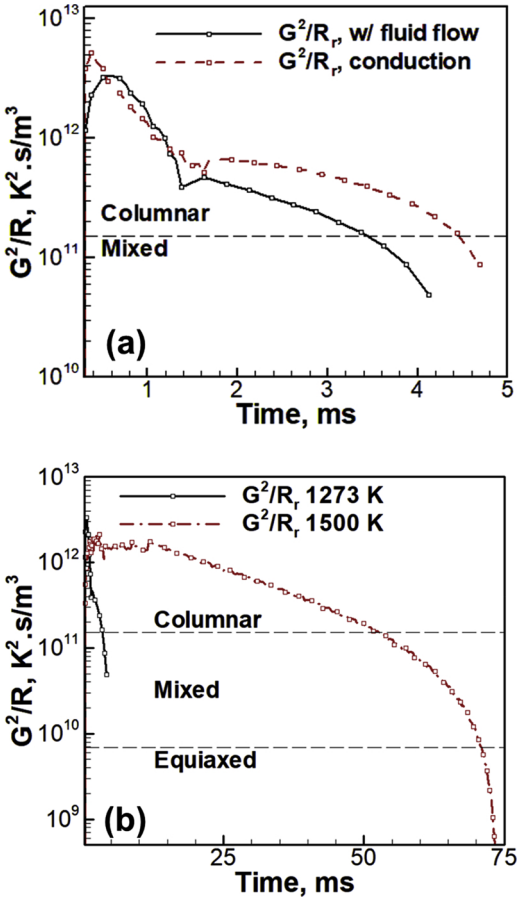

Fig. 9. Transient variation of the CET parameter, G^2/R, during solidification of a single molten pool, calculated from G_r and R_r. (a) Comparison of the parameters with and without fluid flow. (b) Simulations with fluid flow and initial temperature of 1273 K are compared to simulations with an initial temperature of 1500 K to simulate the low and high input energy density samples, respectively. X-axis starts at 0.25 ms, when the beam is turned off.

These changes in G and R lead to significant changes in the derived solidification parameters. Within the first millisecond of cooling after 0.25 ms of melting, the instantaneous cooling rate at the solid/mushy interface, GR, goes from 10^5 K/s to 10^4 K/s, as shown in Fig. 8a. This time period corresponds with the presence of the single-phase liquid region and dominance of convective heat transfer. G/R and G^2/R are also affected, and these changes are discussed in terms of the solidification morphology and CET.

3.3. Solidification morphology

From Eq. (12), it is clear that the CET is sensitive to G^2/R, so the transient aspect of the solidification parameters G and R have potential to induce CET during the solidification of molten pool. As noted earlier, G decreases by an order of magnitude throughout the solidification of a single melted spot, while R only increases by a fraction of an order of magnitude. This ultimately means that G^2/R should decrease over time, meaning a transition from columnar to equiaxed dendrite morphology is possible.

The values of G/R shown in Fig. 8b satisfy the constitutional supercooling criteria in Eq. (5) for cellular/dendritic solidification morphology to form during solidification. Experimental results showed dendrites in both samples, supporting these calculations. Calculation of G^2/R by Eq. (12) enables calculation of temporal variation in equiaxed or columnar dendrite formation. First, the influence of fluid flow is shown in Fig. 9a for the simulation of the lower energy density sample. The magnitude of G^2/R is a factor of approximately three times higher when fluid flow is ignored, due to fluid flow's previously discussed influences on the temperature gradient and solidification rates. Additionally, the solidification varies temporally, affecting the spatial distribution of probable equiaxed dendrites when fluid flow is ignored. These differences are significant because the processing window for PBF-EB lies near equiaxed transition [6], so in cases where equiaxed grains should be suppressed ignoring fluid flow could change predicted microstructures.

Fig. 9b shows the simulated results of G^2/R for the two samples analyzed by EBSD in Fig. 10. The increased spot density for the sample showing equiaxed dendrites increases the amount of heat put into a certain unit area, and therefore increases the accumulated heat in the surrounding substrate. From the simulations, time for a single spot to solidify increases by an order of magnitude when increasing the temperature of the substrate from 1273 K to 1500 K. This significantly affects both the temporal variation in temperature gradients and solidification rates and changes the solidification morphology from columnar to be either mixed or equiaxed morphology. When the material surrounding the molten pool increases in temperature, the overall temperature gradients and G^2/R decrease such that equiaxed grains are more likely to form due to a larger undercooled region. Additionally, the much longer solidification time means that there is potential for multiple spots to join together when processing a part via PBF-EB, creating larger pools with lower temperature gradients and an increased likelihood to form equiaxed grains as shown by Plotkowski

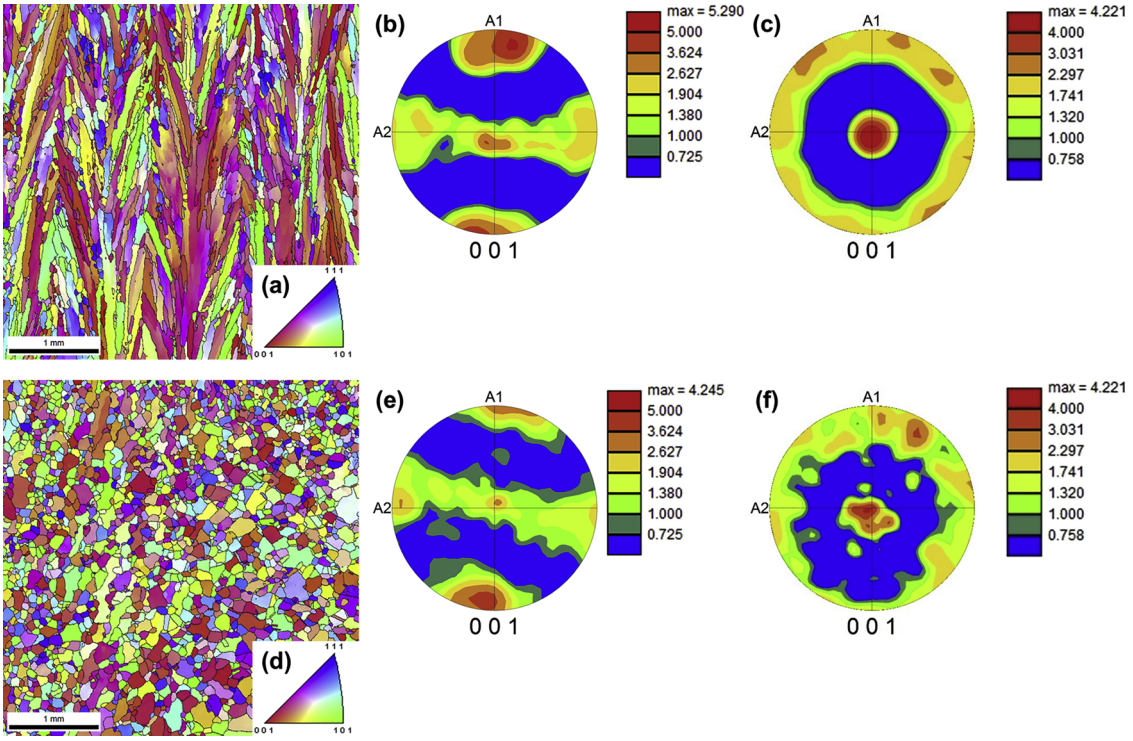

Fig. 10. EBSD results for the experimental specimens. (a–c) 16 spots/mm^2 sample: (a) orientation map for the XZ-plane through the middle of the sample; (b) (001) pole map for the XZ-plane plane shown in (a); (c) (001) pole map for XY-plane perpendicular to the build-direction. (d–f) 36 spots/mm^2 sample: (d) orientation map for the XZ-plane through the middle of the sample; (e) (001) pole map for the XZ-plane plane shown in (d); (f) (001) pole map for XY-plane perpendicular to the build-direction.

et al. [14]. This conclusion is supported by observed experimental results in Fig. 10 and clarifies the temporal and spatial variations of similar results by Raghavan et al. [13] that showed increasing the temperature of the substrate had an influence on the CET of IN718. Even within a single, small pool, the transition from columnar to equiaxed dendrites can occur, exposing the complexity that may occur when melting multiple spots in complex scanning patterns. Understanding these basic phenomena helps enable future research in understanding the role of fluid flow in more complex scenarios.

Substrate heating in the simulations makes the mechanism behind the differences in the experimental samples presented in Fig. 10a and d clear. In Fig. 10a, elongated columnar grains can be seen to grow across multiple layers, as each layer is only 50 μm thick. Some smaller grains can be seen, which are likely a mix of out-of-plane columnar grains and stray equiaxed grains. The pole map in Fig. 10b shows an oriented texture, as columnar grains are aligned with the building direction. These grains are confirmed to be oriented columnar grains by the pole map in Fig. 10c, which was taken from a perpendicular section and shows orientation rotated by 90 °. As observed in Fig. 9b, the end of solidification falls into the region of mixed columnar/equiaxed dendrite morphology, so it is predicted that there will be some equiaxed grains in this case. Comparatively, there are relatively few elongated and oriented grains in Fig. 10d, showing that many more unoriented equiaxed dendrites formed during solidification. Because equiaxed grains form in the bulk liquid, they are not necessarily oriented with the temperature gradient like columnar, epitaxial grains. The pole map in Fig. 10e shows a reduction in the orientation with < 001 > compared to Fig. 10b, confirming that there is an increase in misoriented, equiaxed grains. Fig. 10f confirms this, showing an increased amount of misorientation persists in a plane perpendicular to the pole map in Fig. 10e. Seeing both oriented and misoriented grains in the same sample indicate that the solidification morphology was mixed equiaxed and columnar dendrites. This supports the simulated results of Fig. 9b, which show that a majority of the solidification goes through the mixed morphology region. Because of interruption by equiaxed grain growth, the columnar grains are much shorter than those seen in Fig. 10a and are not as obvious solely from looking at the orientation map. For this reason, pole maps are an important tool in determining the grain morphology that occurs during solidification of AM alloys. The work presented in this paper shows that the solidification parameters responsible for the morphology of grains change with time, which can result in CET even on a very short timescale.

4. Summary and conclusion

Solidification characteristics of IN718 alloy by electron beam additive manufacturing were investigated experimentally and theoretically. The key conclusions are summarized below.

1 Experimentally observed changes in solidification from a columnar morphology to a mixed columnar and equiaxed morphology were explained theoretically. Increased cooling times and decreased temperature gradients occur when increasing input energy density, which leads to the columnar-to-equiaxed transition.
2 Mixed columnar and equiaxed dendritic solidification morphology can occur even within a small molten region and short timescale. Experiments showed that in the mixed morphology solidification, columnar grains oriented with the build direction still form, however they are shorter and rarely grow epitaxially through layers like when solidification morphology is mainly columnar.
3 The liquid region solidifies much more quickly than the two-phase mushy zone and for most of the solidification, the molten pool consists solely of the mushy zone. However, fluid flow in the short-lived single-phase liquid region is shown to influence resultant pool geometry and solidification parameters.
4 Despite the small length scale there are noticeably different solidification conditions in the middle of the pool compared to the edge. The center of the molten pool experiences lower temperature

gradients and higher solidification rates, such that it becomes more conducive to equiaxed grain formation than near the edges of the pool.

5 Increasing the initial temperature of the powder bed decreases temperature gradients and solidification growth rates, increasing the probability of equiaxed grain formation. Increasing input energy density consequently increases the temperature of the powder bed and pushes solidification morphology towards being more equiaxed.

Acknowledgements

Research sponsored by the U.S. Department of Energy, Office of Energy Efficiency and Renewable Energy, Industrial Technologies Program, under contract DE-AC05-00OR22725 with UT-Battelle, LLC. We would also like to thank the researchers of Oak Ridge National Lab for their assistance on this work, particularly Prof. S. S. Babu for his interest in this work.

Appendix A. Supplementary data

Supplementary material related to this article can be found, in the online version, at doi:https://doi.org/10.1016/j.addma.2018.12.001.

References

[1] M.J. Donachie, S.J. Donachie, Superalloys: A Technical Guide, 2nd ed., ASM International, United States of America, 2002.
[2] R.C. Reed, The Superalloys : Fundamentals and Applications, Cambridge University Press, Cambridge, United Kingdom, 2008.
[3] J. Raplee, A. Plotkowski, M.M. Kirka, R. Dinwiddie, A. Okello, R.R. Dehoff, S.S. Babu, Thermographic microstructure monitoring in electron beam additive manufacturing, Sci. Rep. 7 (2017) 43554.
[4] R.R. Dehoff, M.M. Kirka, W.J. Sames, H. Bilheux, A.S. Tremsin, L.E. Lowe, S.S. Babu, Site specific control of crystallographic grain orientation through electron beam additive manufacturing, Mater. Sci. Technol. 31 (8) (2015) 931–938.
[5] N. Raghavan, S. Simunovic, R. Dehoff, A. Plotkowski, J. Turner, M. Kirka, S. Babu, Localized melt-scan strategy for site specific control of grain size and primary dendrite arm spacing in electron beam additive manufacturing, Acta Mater. 140 (2017) 375–387.
[6] W.J. Sames, F.A. List, S. Pannala, R.R. Dehoff, S.S. Babu, The metallurgy and processing science of metal additive manufacturing, Int. Mater. Rev. 61 (5) (2016) 315–360.
[7] R.R. Dehoff, M.M. Kirka, F.A. List, K.A. Unocic, W.J. Sames, Crystallographic texture engineering through novel melt strategies via electron beam melting: Inconel 718, Mater. Sci. Technol. 31 (8) (2015) 939–944.
[8] S.S. Babu, N. Raghavan, J. Raplee, S.J. Foster, C. Frederick, M. Haines, R. Dinwiddie, M.K. Kirka, A. Plotkowski, Y. Lee, R.R. Dehoff, Additive manufacturing of nickel superalloys: opportunities for innovation and challenges related to qualification, Metall. Mater. Trans. A (2018).
[9] J.D. Hunt, Steady state columnar and equiaxed growth of dendrites and eutectic, Mater. Sci. Eng. 65 (1) (1984) 75–83.
[10] W. Kurz, B. Giovanola, R. Trivedi, Theory of microstructural development during rapid solidification, Acta Metall. 34 (1986) 823–830.
[11] J.M. Vitek, The effect of welding conditions on stray grain formation in single crystal welds – theoretical analysis, Acta Mater. 53 (1) (2005) 53–67.
[12] M. Gäumann, C. Bezençon, P. Canalis, W. Kurz, Single-crystal laser deposition of superalloys: processing–microstructure maps, Acta Mater. 49 (6) (2001) 1051–1062.
[13] N. Raghavan, R. Dehoff, S. Pannala, S. Simunovic, M. Kirka, J. Turner, N. Carlson, S.S. Babu, Numerical modeling of heat-transfer and the influence of process parameters on tailoring the grain morphology of IN718 in electron beam additive manufacturing, Acta Mater. 112 (2016) 303–314.
[14] A. Plotkowski, M.M. Kirka, S.S. Babu, Verification and validation of a rapid heat transfer calculation methodology for transient melt pool solidification conditions in powder bed metal additive manufacturing, Addit. Manuf. 18 (2017) 256–268.
[15] E. Attar, C. Körner, Lattice Boltzmann model for thermal free surface flows with liquid–solid phase transition, Int. J. Heat Fluid Flow 32 (1) (2011) 156–163.
[16] S. Thorsten, J. Vera, S.R.F.K. Carolin, Influence of the scanning strategy on the microstructure and mechanical properties in selective electron beam melting of Ti–6Al–4V, Adv. Eng. Mater. 17 (11) (2015) 1573–1578.
[17] C. Körner, E. Attar, P. Heinl, Mesoscopic simulation of selective beam melting processes, J. Mater. Process. Technol. 211 (6) (2011) 978–987.
[18] H.L. Wei, J. Mazumder, T. DebRoy, Evolution of solidification texture during additive manufacturing, Sci. Rep. 5 (2015) 16446.
[19] A. Rai, H. Helmer, C. Körner, Simulation of grain structure evolution during powder bed based additive manufacturing, Addit. Manuf. 13 (2017) 124–134.
[20] H. Helmer, A. Bauereiß, R. Singer, C. Körner, Grain structure evolution in Inconel 718 during selective electron beam melting, Mater. Sci. Eng. A 668 (2016) 180–187.
[21] T. DebRoy, H.L. Wei, J.S. Zuback, T. Mukherjee, J.W. Elmer, J.O. Milewski, A.M. Beese, A. Wilson-Heid, A. De, W. Zhang, Additive manufacturing of metallic components – process, structure and properties, Prog. Mater. Sci. 92 (Supplement C) (2018) 112–224.
[22] T. DebRoy, S.A. David, Physical processes in fusion welding, Rev. Mod. Phys. 67 (1) (1995) 85–112.
[23] T. Mukherjee, H.L. Wei, A. De, T. DebRoy, Heat and fluid flow in additive manufacturing—part I: modeling of powder bed fusion, Comput. Mater. Sci. 150 (2018) 304–313.
[24] V. Manvatkar, A. De, T. DebRoy, Heat transfer and material flow during laser assisted multi-layer additive manufacturing, J. Appl. Phys. 116 (12) (2014) 124905.
[25] S. Price, B. Cheng, J. Lydon, K. Cooper, K. Chou, On Process Temperature in Powder-bed Electron Beam Additive Manufacturing: Process Parameter Effects, (2014).
[26] M. Galati, L. Iuliano, A. Salmi, E. Atzeni, Modelling energy source and powder properties for the development of a thermal FE model of the EBM additive manufacturing process, Addit. Manuf. 14 (2017) 49–59.
[27] X. He, T. DebRoy, P.W. Fuerschbach, Probing temperature during laser spot welding from vapor composition and modeling, J. Appl. Phys. 94 (10) (2003) 6949–6958.
[28] S. Mishra, T. DebRoy, A heat-transfer and fluid-flow-based model to obtain a specific weld geometry using various combinations of welding variables, J. Appl. Phys. 98 (4) (2005) 044902.
[29] S. Patankar, Numerical Heat Transfer and Fluid Flow, Hemisphere Publishing Corporation, 1980.
[30] X. He, P.W. Fuerschbach, T. DebRoy, Heat transfer and fluid flow during laser spot welding of 304 stainless steel, J. Phys. D Appl. Phys. 36 (12) (2003) 1388.
[31] N.K. Tolochko, M.K. Arshinov, A.V. Gusarov, V.I. Titov, T. Laoui, L. Froyen, Mechanisms of selective laser sintering and heat transfer in Ti powder, Rapid Prototyp. J. 9 (5) (2003) 314–326.
[32] R.F. Brooks, B. Monaghan, A.J. Barnicoat, A. McCabe, K.C. Mills, P.N. Quested, The physical properties of alloys in the liquid and “mushy” states, Int. J. Thermophys. 17 (5) (1996) 1151–1161.
[33] B.P. Keller, S.E. Nelson, K.L. Walton, T.K. Ghosh, R.V. Tompson, S.K. Loyalka, Total hemispherical emissivity of Inconel 718, Nucl. Eng. Des. 287 (2015) 11–18.
[34] S. Schiller, U. Heisig, S. Panzer, Electron Beam Technology, Wiley, New York, 1982.
[35] R. Rai, T. Palmer, J. Elmer, T. Debroy, Heat transfer and fluid flow during electron beam welding of 304L stainless steel alloy, Weld. J. 88 (3) (2009) 54–61.
[36] U. Dilthey, A. Goumeniouk, O. Nazarenko, K. Akopjantz, Mathematical simulation of the influence of ion-compensation, self-magnetic field and scattering on an electron beam during welding, Vacuum 62 (2-3) (2001) 87–96.
[37] Thermochemical data, in: W.F. Gale, T.C. Totemeier (Eds.), Smithells Metals Reference Book (Eighth Edition), Butterworth-Heinemann, Oxford, 2004, pp. 8.1–8.58.
[38] P. Sahoo, M.M. Collur, T. Debroy, Effects of oxygen and sulfur on alloying element vaporization rates during laser welding, Metall. Trans. B 19 (6) (1988) 967–972.
[39] A. Block-Bolten, T. Eagar, Metal vaporization from weld pools, Metall. Trans. B 15 (3) (1984) 461–469.
[40] Special Metals Corporation, INCONEL® Alloy 718, Publication Number SMC-045, (2007), pp. 1–28.
[41] S. Kou, Welding Metallurgy, 2nd ed., Wiley-Interscience, Hoboken, N.J, 2003.
[42] L. Nastac, D.M. Stefanescu, Macrotransport-solidification kinetics modeling of equiaxed dendritic growth: Part II. Computation problems and validation on INCONEL 718 superalloy castings, Metall. Mater. Trans. A 27 (12) (1996) 4075–4083.
[43] L. Nastac, D.M. Stefanescu, Macrotransport-solidification kinetics modeling of equiaxed dendritic growth: Part I. Model development and discussion, Metall. Mater. Trans. A 27 (12) (1996) 4061–4074.
[44] M. Gäumann, R. Trivedi, W. Kurz, Nucleation ahead of the advancing interface in directional solidification, Mater. Sci. Eng. A 226 (1997) 763–769.
[45] W. Kurz, C. Bezencon, M. Gäumann, Columnar to equiaxed transition in solidification processing, Sci. Technol. Adv. Mater. 2 (1) (2001) 185–191.
[46] L. Nastac, J.J. Valencia, M.L. Tims, F.R. Dax, Advances in the solidification of IN718 and RS5 alloys, in: E.A. Loria (Ed.), Superalloys 718, 625, 706 and Various Derivatives, The Minerals, Metals & Materials Society, 2001, pp. 103–112.
[47] T.A. Palmer, J.W. Elmer, Characterisation of electron beams at different focus settings and work distances in multiple welders using the enhanced modified Faraday cup, Sci. Technol. Weld. Join. 12 (2) (2007) 161–174.
[48] T. Mukherjee, V. Manvatkar, A. De, T. DebRoy, Dimensionless numbers in additive manufacturing, J. Appl. Phys. 121 (6) (2017) 064904.
[49] W. Zhang, G.G. Roy, J.W. Elmer, T. DebRoy, Modeling of heat transfer and fluid flow during gas tungsten arc spot welding of low carbon steel, J. Appl. Phys. 93 (5) (2003) 3022–3033.